Universidade de São Paulo
Biblioteca Digital da Produção Intelectual - BDPI

Departamento de Física e Ciência Interdisciplinar - IFSC/FCI Artigos e Materiais de Revistas Científicas - IFSC/FCI

2014-07

White light and multicolor emission tuning in triply doped Yb3+/Tm3+/Er3+ novel fluoro-phosphate transparent glass-ceramics

Journal of Materials Chemistry C, Cambridge : Royal Society of Chemistry - RSC, v. 2, n. 25, p. 5046-5056, July 2014
http://www.producao.usp.br/handle/BDPI/50217

Downloaded from: Biblioteca Digital da Produção Intelectual - BDPI, Universidade de São Paulo

Journal of Materials Chemistry C

ROYAL SOCIETY OF CHEMISTRY

PAPER

View Article Online
View Journal | View Issue

Published on 07 April 2014. Downloaded by UNIVERSIDAD SAO PAULO on 23/06/2014 15:15:39.

Cite this: J. Mater. Chem. C, 2014, 2, 5046

White light and multicolor emission tuning in triply doped $Yb^{3+}/Tm^{3+}/Er^{3+}$ novel fluoro-phosphate transparent glass-ceramics

Yannick Ledemi,*[a] Andrée-Anne Trudel,[a] Victor A. G. Rivera,[b] Sébastien Chenu,[c] Emmanuel Véron,[c] Luiz Antonio Nunes,[b] Mathieu Allix[c] and Younès Messaddeq[a]

Received 7th March 2014
Accepted 5th April 2014

DOI: 10.1039/c4tc00455h

www.rsc.org/MaterialsC

New Yb^{3+}, Er^{3+} and Tm^{3+} doped fluoro-phosphate glasses belonging to the system $NaPO_3$–YF_3–BaF_2–CaF_2 and containing up to 10 wt% of rare-earth ion fluorides were prepared and characterized by differential scanning calorimetry, absorption spectroscopy and up-conversion emission spectroscopy under excitation with a 975 nm laser diode. Transparent and homogeneous glass-ceramics have been reproducibly obtained with a view to manage the red, green and blue emission bands and generate white light. X-ray diffraction as well as electron microscopy techniques have confirmed the formation of fluorite-type cubic nanocrystals at the beginning of the crystallization process while complex nanocrystalline phases are formed after a longer heat-treatment. The prepared glass-ceramics exhibit high optical transparency even after 170 h of thermal treatment. An improvement of up-conversion emission intensity – from 10 to 160 times larger – was measured in the glass-ceramics when compared to the parent glass, suggesting an important incorporation of the rare-earth ions into the crystalline phase(s). The involved mechanisms and lifetime were described in detail as a function of heat-treatment time. Finally, a large range of designable color rendering (from orange to turquoise through white) can be observed in these materials by controlling the laser excitation power and the crystallization rate.

1. Introduction

Tailoring the emission of light in the ultraviolet, visible and/or the infrared ranges has always been a challenge of material research due to its numerous applications in optic and photonic devices for solid-state lighting and lasers, multicolor displays technology, and more recently to improve the solar cell efficiency.[1–3] Among the different routes explored for such purposes, including inorganic and organic semi-conductor technologies and transition metal or lanthanide ion doped single crystals or ceramics, the use of glass as an active material offers many advantages. We can cite the optical transparency in the range of interest, ease of preparation associated with a relatively low-cost production as well as ease of shaping in the desired form (*e.g.* thin-films, optical fibers) depending on the targeted application. Besides, growing interest over the past decade has been observed in the field of transparent glass-ceramic materials for optic and photonic applications. For a long time, the interest in these composite materials has originated from their excellent thermo-mechanical properties.[4] Nevertheless, constant efforts have been devoted to the improvement of their optical transparency leading progressively to new applications for glass-ceramics as photonic materials.[5–7] The recent advances in the controlled crystallization process of glasses permit us to manage the size and nature of crystals within the vitreous matrix, and thus to master the light scattering. Nowadays, considerable research is dedicated to the preparation of new optical glass-ceramics from photonic glasses (*e.g.* oxyfluorides,[5,6] chalco-halides,[7] fluorosilicates,[8,9] *etc.*) with a view to combine the specific glass features to the unique properties of single crystals.

Among the numerous photonic applications (*e.g.* laser amplification, saturable absorbers, frequency doubling, lens, *etc.*), transparent luminescent glass-ceramics may exhibit enhanced optical properties (*e.g.* absorption/emission cross-section, energy transfer rates) compared to their glassy counterparts when a crystalline phase of the desired nature and structure is generated around the active species, usually rare earth ions (REI) or transition metal ions.[6,10] In some cases, the own crystals themselves are the emitting species, like in quantum dot doped glasses.[11] One of the most explored methods is the incorporation of efficient up-converter nano-crystals within the glassy network. Nano-crystalline materials such as $NaYF_4$, YF_3 or CaF_2 doped with lanthanide ions are known to be highly efficient up-converters and have already

[a]Centre d'Optique, Photonique et Laser, Université Laval, 2375 rue la Terrasse, Québec (Qc), G1V 0A6, Canada
[b]Instituto de Física de São Carlos – INOF, USP, Caixa Postal 369, 13560-970, São Carlos, SP, Brazil
[c]Conditions Extrêmes et Matériaux: Haute Température et Irradiation, CEMHTI-CNRS UPR3079, 1D avenue de la Recherche Scientifique, 45071, Orléans Cedex 2, France

This journal is © The Royal Society of Chemistry 2014

Published on 07 April 2014. Downloaded by UNIVERSIDAD SAO PAULO on 23/06/2014 15:15:39.

found applications in biology and medical imaging.[9,12–15] By tailoring their crystalline structure, relatively low-symmetry sites can be formed, resulting in a distortion of the electron cloud around the REI and favoring thus their emission features.[16] When the concentrations of REI such as Yb^{3+} as the sensitizer ion and Er^{3+}, Tm^{3+}, Ho^{3+} and/or Pr^{3+} as activator ions are appropriately adjusted in these nanocrystals, efficient multicolor and white light emission through red–green–blue (RGB) combination can be achieved usually by simple excitation with a commercial 980 nm laser diode.[15,17–19] Owing to their high potential as an alternative source for lighting, laser or sensing, great interest has thus emerged in investigating beyond the extensively studied REI doped glassy materials[20–23] by embedding their REI into up-converter nanocrystals and forming more efficient active glass-ceramics.[24–26] The main part of the vitreous materials explored with a view to prepare these luminescent glass-ceramics is based on oxyfluoride mixed glass systems such as fluoro-germanate[27–29] or fluoro-alumino-silicate.[30–35] In a previous study, we have reported an enhanced up-conversion emission in Yb^{3+} and Er^{3+} co-doped $NaPO_3$–YF_3–BaF_2–CaF_2 fluoro-phosphate glass-ceramics.[36] Basically, the incorporation of both REI into fluorite type nanocrystals increases their proximity, favoring the energy transfer from the Yb^{3+} acceptor ions to the Er^{3+} activator ones, thus improving their visible luminescence.

In this work, we study the infrared to visible up-conversion emission in Yb^{3+}, Tm^{3+} and Er^{3+} triply doped $NaPO_3$–YF_3–BaF_2–CaF_2 fluoro-phosphate glasses and transparent glass-ceramics. Through a well-controlled and highly reproducible crystallization process, glass-ceramics containing fluorite-type nanocrystals homogeneously dispersed within the volume have been fabricated. From these REI doped transparent glass-ceramics, significant changes in the relative intensities of the violet, blue, green and red emissions upon 975 nm laser diode excitation have been observed as a function of the applied heat-treatment duration and laser excitation power. Such features are attributed to the incorporation of REI into the nanocrystals and give rise to a large range of color tunability passing over the white light from a single bulk material, according to the CIE-1931 standards.[37] Moreover, a large enhancement of the up-conversion emission intensity as well as their corresponding lifetimes has been observed and correlated with the structural changes occurring along the controlled crystallization process.

2. Experimental section

Glasses with nominal composition $(NaPO_3)_{40}$–$(YF_3)_{30}$–$(BaF_2)_{20}$–$(CaF_2)_{10}$ (mol%) of 10 g weight and triply doped with 4 wt% of ytterbium fluoride (YbF_3), 2 wt% of erbium fluoride (ErF_3) and different amounts of thulium fluoride (TmF_3) ($x = 1$, 2, 3 and 4 wt%) were prepared by the traditional melt-casting technique and annealed below their glass transition temperature (T_g) to remove any residual internal stress induced by the rapid cooling of the glass melt. More details about the preparation route are given in our previous work[36] and the studied glass samples are labeled in the text NYBC-x with x the weight concentration of TmF_3.

Glass-ceramics have been prepared by thermal treatment at 380 °C (20 °C above glass transition temperature) for different durations of the selected parent glass composition, according to the same procedure detailed in.[36] One can note that an excellent repeatability of glass-ceramics preparation was observed from different parent glasses of the same composition according to the used process. For clarity, the studied glass-ceramics are labeled in the text GC-y h with y the heat-treatment duration (in hours) at 380 °C.

The crystallization of the glass $(NaPO_3)_{40}$–$(YF_3)_{30}$–$(BaF_2)_{20}$–$(CaF_2)_{10}$ triply doped Yb^{3+}, Er^{3+} and Tm^{3+} was studied by *in situ* high-temperature X-ray diffraction (HT-XRD), using an Anton Paar oven Chamber (model HTK1200N, Graz, Austria) based on a Kanthal® resistive heating attachment. Diffraction data were collected over the 15–70° 2θ range with a 0.0245° step (4 s per step counting time) on an X-ray Bruker D8 Advance ($CuK\alpha_{12}$ radiation) equipped with a Vantec-1 linear detector. The powder or bulk sample was placed on a corundum crucible covered by a platinum pellet to minimize interaction. The sample temperature was previously calibrated using the thermal expansion of Al_2O_3.[38] The sample was heated from room temperature to 380 °C at a rate of 10 K min^{-1} and diffractograms were collected for one hour from $t = 0$ to $t = 85$ h. The differential scanning calorimetric (DSC) measurements were performed using a Netzsch DSC Pegasus 404F3 apparatus on glass pieces into sealed Al pans at a heating rate of 10 °C min^{-1}.

The scanning electron microscopy (SEM) images were obtained by using a FEI Quanta 3D microscope equipped with a Field Emission Gun (FEG). The bulk samples were fractured purposely prior to SEM imaging to allow both surface and volume observations. The low vacuum observation mode for this dielectric material was preferred to dispense with sample metallization which usually shows specific texture at high rates of magnification. In return the image contrast obtained under this mode is not as high as that of metallized (dielectric) samples observed under high vacuum. Transmission Electron Microscopy (TEM) data were collected on a Philips CM20 microscope fitted with an Oxford Energy Dispersive Spectrometry (EDS) analyzer. The sample was first crushed in ethanol, and a drop of the solution with small crystallites in suspension was deposited onto a carbon coated copper grid.

The digital photographs of the samples were taken with a Sony Cybershot digital camera DSC-W85 by holding them about 5 cm above a text instead of lying on it to better show their optical transparency.

The UV-visible transmission spectra were recorded on a Cary 500 (Varian) double beam spectrophotometer on the polished samples of 1.5 mm thickness. The linear refractive index was measured by employing the M-lines prism coupling technique (Metricon 2010) at 633 nm. The steady state fluorescence emission spectra were recorded by using a Nanolog Horiba Jobin Yvon fluorimeter equipped with a double monochromator and a photomultiplier tube (PMT) sensitive from 250 to 850 nm. A laser diode operating at 975 nm coupled with a standard monomode pigtailed fiber (SMF28) and the collimated laser excitation beam was focused on the sample surface through an 18.4 mm lens. All measurements were performed at room

Published on 07 April 2014. Downloaded by UNIVERSIDAD SAO PAULO on 23/06/2014 15:15:39.

temperature. Further details about the conditions and precautions used for the luminescence measurements can be found in ref. 36. In addition to the steady state measurements, time resolved experiments were also performed to find out the excited states lifetime under excitation at 980 nm by using an OPO laser pumped by the 3rd harmonic of a Nd:YAG laser, with a peak power of 50 kW, a pulse width of 5 ns and a time between 2 pulses of 5 ms. The emission signal was recorded on a 400 MHz oscilloscope (Tektronix TDS 380) and the lifetime data were fitted using the expression: $I(t) = I_0 \exp[-t/\tau]$, where τ is the relaxation time and I_0 is the intensity at time zero.

3. Results

3.1 The glasses

In a first step, the concentration of doping rare earth ions Yb^{3+}, Er^{3+} and Tm^{3+} was explored in order to achieve white light emission, thanks to a combination of the green and red emissions of Er^{3+} ions and the blue and red emissions of Tm^{3+} ions after excitation at 975 nm with a laser diode.[15,17–19] The involved mechanisms will be described later in the text. The concentration of TmF_3 in the glass of nominal composition $(NaPO_3)_{40}$–$(YF_3)_{30}$–$(BaF_2)_{20}$–$(CaF_2)_{10}$ (mol%) was varied from 1 to 4 wt% while the concentrations of YbF_3 and ErF_3 were maintained constant at 4 wt% and 2 wt%, respectively. The glasses prepared with different amounts of TmF_3 are optically homogeneous, without evidence of crystallization or striae. Their emission spectra recorded from 370 to 850 nm upon excitation at 975 nm (diode power of 25 mW) are presented in Fig. 1. The recorded emission spectra were normalized at 549 nm, which is the main radiative transition of Er^{3+} ions whose concentration was kept constant in the four samples, helping thus to better account for the Tm^{3+} ion contribution through its blue emission at 478 nm. The coordinates for each sample in the chromaticity diagram (CIE-1931)[37] are shown in the inset of Fig. 1, after calculation from their emission spectra in the visible region, *i.e.* from 380 to 720 nm, by using the Spectra Lux software.[39] The six emission bands observed in the spectra in Fig. 1 can be assigned as follows: (i) the 520, 540, 667 and 810 nm bands originate from the Er^{3+} radiative transitions from the excited state $^2H_{11/2}$, $^4S_{3/2}$, $^4F_{9/2}$ and $^4I_{9/2}$ to the ground state $^4I_{15/2}$, respectively, and, (ii) the 478 and 795 nm bands are due to Tm^{3+} direct radiative transitions from the excited state $^1G_4$ and $^3H_4$ to the ground state $^3H_6$, respectively, while the 450 and 651 nm bands correspond to indirect transitions from the excited state $^1D_2$ and $^1G_4$ to the excited state $^3F_4$, respectively. One can observe in Fig. 1 that increasing the Tm^{3+} concentration results in: (i) a monotonous decrease of the relative intensity of the blue emission at 478 nm, attributed to Tm^{3+} ion transition which will be described later and (ii) a slight increase of the red emission intensity at 651 nm. This leads to a different color rendering of the emission from bluish to white of the glass samples according to their Tm^{3+} content, as depicted in the inset of Fig. 1 and shown on the photographs of the glass samples under excitation at 975 nm (diode power of 30 mW, focal lens: 50 mm) presented in Fig. 1.

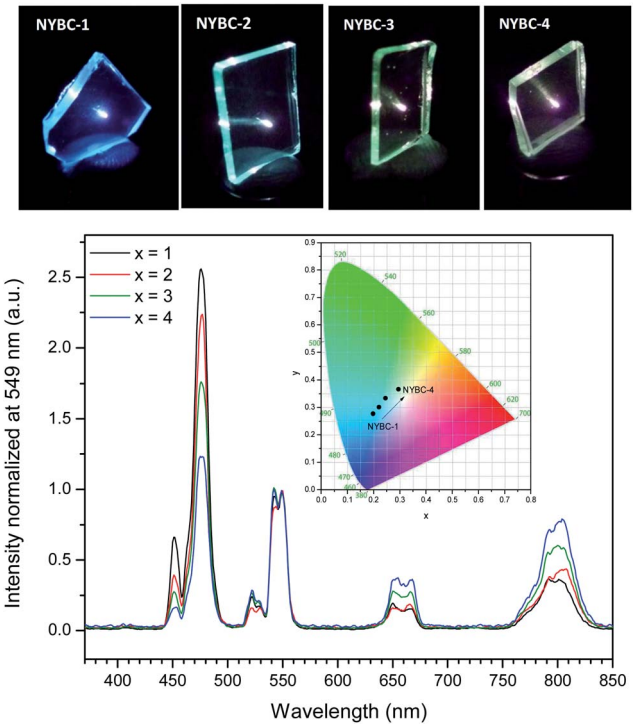

Fig. 1 Normalized up-conversion emission spectra of the NYBC-*x* (with $x = 1$, 2, 3 and 4) glasses as a function of Tm^{3+} concentration, under excitation at 975 nm (diode power of 25 mW). Inset: chromaticity diagram with the calculated corresponding coordinates. Photographs of the NYBC-*x* glass samples under excitation at 975 nm (diode power of 30 mW, focal lens: 50 mm).

3.2 The glass-ceramics

The rare earth ion concentrations, 4 wt% of YbF_3, 2 wt% of ErF_3 and 4 wt% of TmF_3, appear thus as the best REI combination for the emission of white light under 975 nm laser excitation in the $(NaPO_3)_{40}$–$(YF_3)_{30}$–$(BaF_2)_{20}$–$(CaF_2)_{10}$ glass. The NYBC-4 glass was therefore selected as the parent glass composition for the preparation of glass-ceramics by thermal treatment. The NYBC-4 glass-ceramics were obtained by heat-treatment at 380 °C, which is a temperature above its glass transition temperature ($T_g = 361$ °C), and below its onset crystallization temperature ($T_x = 408$ °C), for various durations ranging from 1 to 170 h. The transmission spectra in the ultraviolet to near-infrared range of the prepared glass-ceramics are presented in Fig. 2 as a function of heat-treatment duration. As observed in these spectra, the transparency of the glass-ceramics is altered with increasing heat-treatment time in two ways due to scattering losses induced by the formation and growth of crystals within the glass network, as illustrated by the inset photograph in Fig. 2.

Firstly, the ultraviolet cut-off wavelength is red-shifted, *e.g.* from 308 to 576 nm for 50% of transmission for the glass and GC-170 h samples, respectively, and also accompanied by a curvature of the top of the transmission edge. Secondly, the maximum transmission in the near-infrared range slightly decreases with increasing heat-treatment time, *e.g.* from 90% to 83% between the Tm^{3+}: $^3H_5$ and Er^{3+}: $^4I_{13/2}$ absorption bands for the glass and the glass-ceramic treated 170 h, respectively. Both

 This journal is © The Royal Society of Chemistry 2014

Published on 07 April 2014. Downloaded by UNIVERSIDAD SAO PAULO on 23/06/2014 15:15:39.

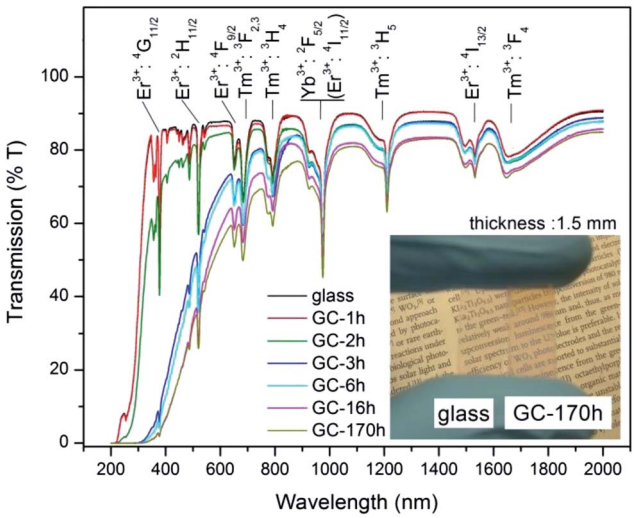

Fig. 2 UV-visible and near infrared transmission spectra of the NYBC-4 glass and glass-ceramics as a function of heat-treatment time at 380 °C. Sample thickness is 1.5 mm. Inset: photograph of NYBC-4 glass and GC-170 h glass-ceramic samples. Note that both samples are held about 5 cm above a text instead of lying on it to better show their optical transparency.

effects can be explained by the presence in the transparent glassy matrix of scattering centers whose concentration, dimensions and/or shape evolve with increasing heat-treatment time. It is worth noting that, on one hand, almost no change occurs in the sample transmission spectrum after 1 h of heat-treatment and, on the other hand, little change occurs between 16 h and 170 h of heat-treatment.

The *in situ* X-ray diffraction patterns recorded on the glass and glass-ceramics every hour (from 0 to 85 h) under heat-treatment at 380 °C are presented in Fig. 3. Despite the fact that the same temperature as that of GC-*y* h preparation was used to record the *in situ* XRD patterns, one might expect some little variation in the crystallization behavior caused by the furnace temperature difference and used sample form (*in situ* XRD patterns were recorded on powder).

However, one can observe very good agreement of the *in situ* and *ex situ* (recorded on crushed glass-ceramics) XRD patterns, as shown in Fig. 3(a) and (b). Besides this confirms that the nucleation process of the NYBC glass is highly homogeneous (volume crystallization). It also supports that possible variation such as treatment duration offsets (related to crystallization kinetics) can be neglected here to simplify the correlation between the structural and optical properties of the GCs.

One can observe in Fig. 3(a) that the XRD pattern of the glass powder is characteristic of its amorphous state ($t = 0$ h). Then, the crystallization process can be divided into four regimes, successively identified by labels (i) to (iv) in both Fig. 3(a) and (b).

First, from 1 h to about 3 h of thermal-treatment (labeled (i) in Fig. 3), four intense distinct peaks are clearly observed at the same angles ($2\theta \approx 28°$, 32°, 46° and 54°). The maximal intensity of these peaks is reached at the very beginning of the crystallization process (after 1 h) and seems constant for about 3 h of treatment, indicating that the corresponding crystal phase is formed very early and rapidly in this regime. Quick XRD extra measurements (not presented here) have shown that this maximal intensity is actually attained after 30 min of thermal treatment at 380°. Indexation of these peaks from the International Centre for Diffraction Data (ICDD) database reveals the presence of possibly three isomorphs cubic fluorite-type phases: sodium yttrium fluoride $NaYF_4$ (JCPDF file 77-2042), calcium fluoride CaF_2 (JCPDF file 35-0816) and calcium yttrium fluoride $Ca_{1-x}Y_xF_{2+x}$ (JCPDF file 31-0293). Extensive structural investigations are currently in progress in order to identify the nature of the crystallizing phase(s). In a second regime ranging approximately from 3 h to 18 h of thermal-treatment at 380 °C (labeled (ii) in Fig. 3), four new peaks are rising at $2\theta \approx 27°$, 31°, 44.5° and 52.5° while the intensity of the four peaks previously

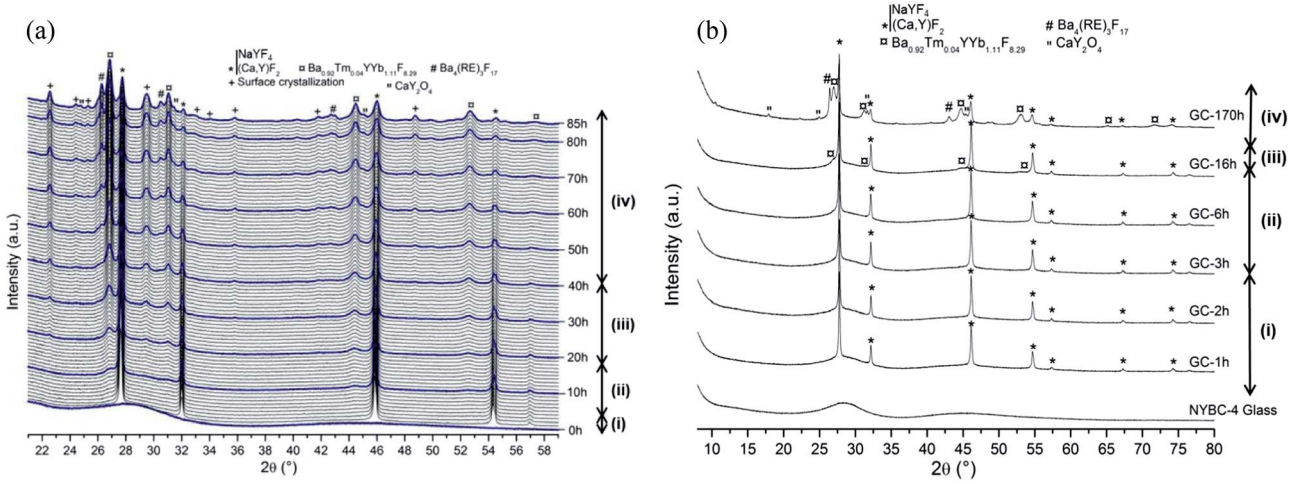

Fig. 3 (a) *In situ* powder X-ray diffraction patterns of the NYBC-4 glass and glass-ceramics every hour from $t = 0$ to $t = 85$ h at 380 °C (1 h scans). Labels (i) to (iv) indicate the four successive regimes of crystallization described in the text. (b) X-ray powder diffraction patterns of the NYBC-4 glass and glass-ceramics obtained after thermal treatment at 380 °C during 1 h, 2 h, 3 h, 6 h, 16 h and 170 h. Labels (i) to (iv) indicate the four successive regimes of crystallization described in the text.

Published on 07 April 2014. Downloaded by UNIVERSIDAD SAO PAULO on 23/06/2014 15:15:39.

observed tends to decrease slowly. The new peaks can be ascribed to the $Ba_{0.92}Tm_{0.04}Y_1Yb_{1.11}F_{8.29}$ crystal phase (JCPDF file 49-0287) which is a face centered cubic structure.[40] In a third regime ranging from 18 h to 40 h (labeled (iii) in Fig. 3), three weak peaks are rising at $2\theta \approx 22.5°$, 29.5° and 36°. However, these peaks are almost not observable in the *ex situ* XRD pattern, *i.e.* from the crushed bulk glass-ceramic samples, as shown in Fig. 3(b). This suggests thus that some surface crystallization occurs during the *in situ* experiment performed on powders. Lastly, above 40 h of heat-treatment (labeled (iv) in Fig. 3), the intensity of the four peaks observed from the beginning still decreases continuously, as clearly observed in Fig. 3 (at $2\theta \approx 28°$, 32°, 46° and 54°). Moreover, different growing peaks are observed in this fourth regime (at $2\theta \approx 26.3°$, 30.5° and 43°). Their complete indexation is rather complex, but could be attributed to the formation of the rhombohedral $Ba_4Yb_3F_{17}$ and/or the orthorhombic CaY_2O_4 phases.

Fig. 4 shows transmission and scanning electron micrographs of the NYBC-4 glass and glass-ceramics GC-1 h, GC-2 h, GC-6 h and GC-170 h. The TEM image in Fig. 4(a) clearly illustrates the homogeneous amorphous character of the NYBC-4 glass sample. In Fig. 4(b)–(f), one can observe crystals of about 100 nm size randomly dispersed in the glassy matrix. No significant difference in terms of crystal size and concentration is observed between the micrographs.

The up-conversion emission spectra from 380 to 850 nm of the NYBC-4 parent glass are presented in Fig. 5 as a function of laser diode power at 975 nm. One has to remind that the laser diode power reported is much lower than the effective power arriving at the sample surface after collimation and tight focusing, as discussed in our previous work.[36] One can observe the same six emission bands at 450, 478, 520, 540, 651 and 795 nm, previously ascribed to the Er^{3+} and Tm^{3+} radiative transitions. Their dependence on the maximum intensity as a function of excitation power is also depicted through a double log–log plot in the inset of Fig. 5.

In the same way, the up-conversion emission spectra from 380 to 850 nm of the NYBC-4 glass-ceramic GC-170 h are presented in Fig. 6 as well as the dependence on the pump power of the maximum intensity of the bands centered at 406, 478, 520, 540, 651 and 795 nm. Besides an increase of about one order of magnitude of the overall emission intensity of the GC-170 h sample when compared to the glass one (see Fig. 5), it is interesting to note the rising of the violet radiative transition of Er^{3+}: $[^2H_{9/2} \rightarrow {}^4I_{15/2}]$ ions at 406 nm in the glass-ceramic emission spectra, while its intensity is negligible on the glass emission spectra.

Furthermore, significant changes in the relative intensities of the different emission bands can be observed in the emission spectra of the glass and GC-170 h glass-ceramic presented in Fig. 5 and 6, respectively. These variations have been summarized in Fig. 7 by plotting the ratio of the intensities measured on the glass-ceramic over that of glass as a function of heat-treatment time and for each emission band. Note that a log–log scale has

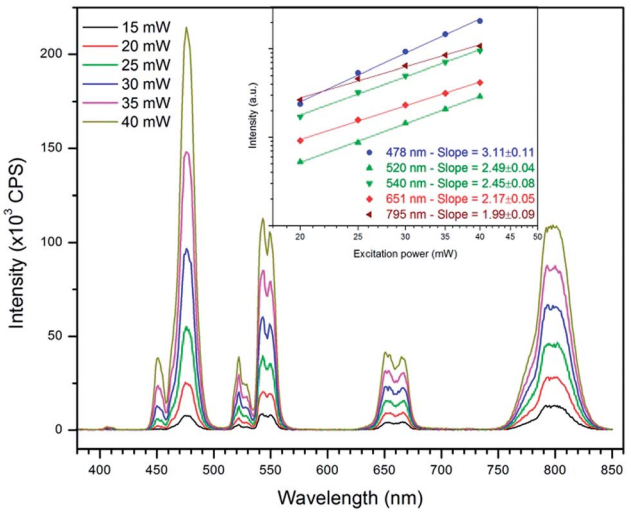

Fig. 5 Up-conversion emission spectra of the NYBC-4 glass as a function of laser diode pump power at 975 nm. Inset: log–log plot of the emission intensity as a function of excitation power.

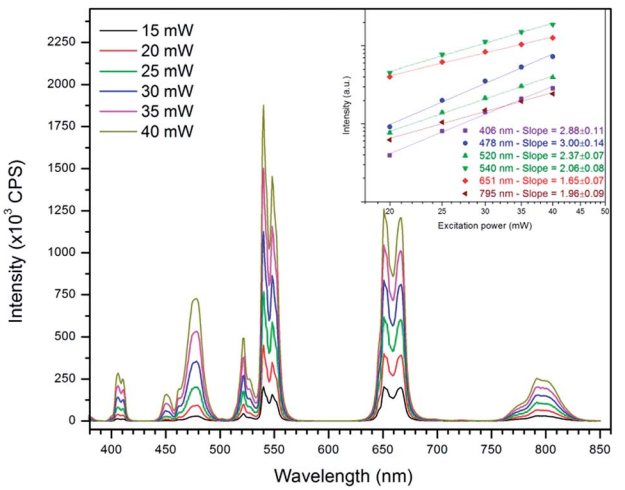

Fig. 6 Up-conversion emission spectra of the NYBC-4 glass-ceramic GC-170 h as a function of laser diode pump power at 975 nm. Inset: log–log plot of the emission intensity as a function of excitation power.

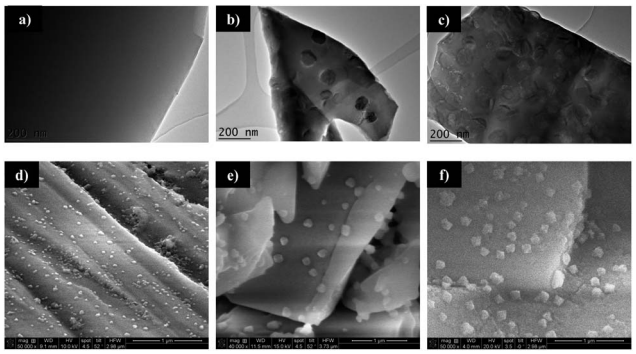

Fig. 4 Transmission Electron Microscopy (TEM) images of NYBC-4 glass (a), glass-ceramics GC-1 h (b) and GC-2 h (c); and Scanning Electron Microscopy (SEM) images of glass-ceramics GC-2 h (d), GC-6 h (e) and GC-170 h (f).

This journal is © The Royal Society of Chemistry 2014

Published on 07 April 2014. Downloaded by UNIVERSIDAD SAO PAULO on 23/06/2014 15:15:39.

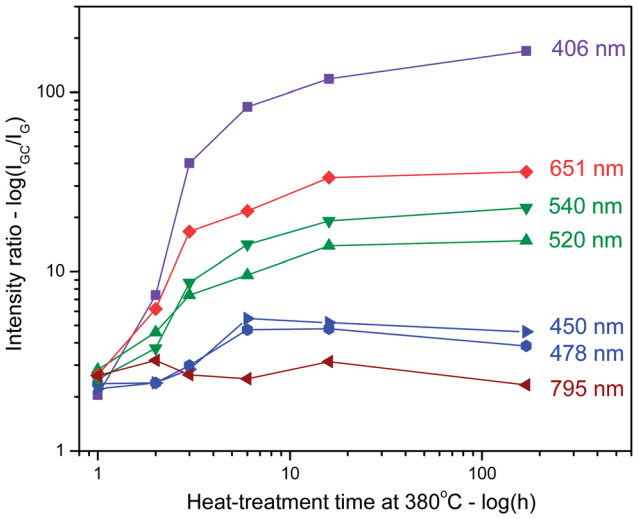

Fig. 7 Ratios (log scale) of the measured emission intensity of the NYBC-4 glass-ceramics over the glass one for each emission band, under excitation at 975 nm (diode power of 30 mW) as a function of heat-treatment time (log scale). Lines are guides to the eye.

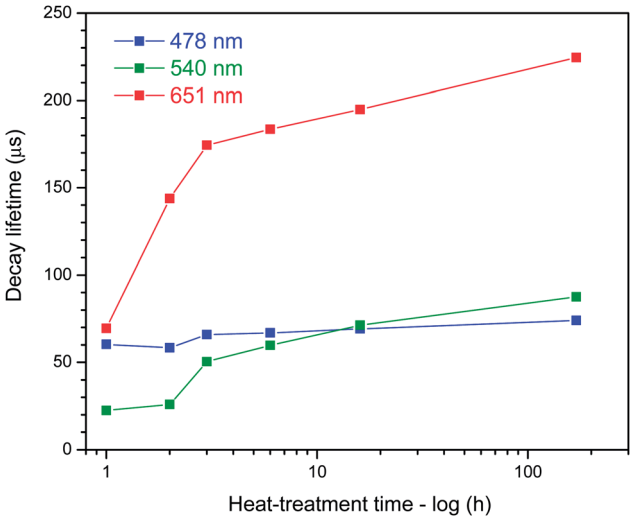

Fig. 8 Decay lifetime (normal scale) of the 478, 540 and 651 nm emission bands under excitation at 980 nm as a function of heat-treatment time (log scale). Lines are guides to the eye.

been preferred in Fig. 7 to better represent the evolution of the intensity ratio as a function of heat-treatment duration.

First, one can observe in Fig. 7 a monotonous and tremendous increase – up to 170 times – of the intensity for the 406 nm emission of Er^{3+} ions with increasing heat-treatment time. Then, a moderate increase of intensity ranging from 10 to 35 times is observed for the 520, 540 and 651 nm Er^{3+} emission bands for the glass-ceramic GC-16 h while no further increase was measured for longer heat-treatment. Lastly, no significant change in intensity was measured for the 478 and 795 nm emission bands relative to the Tm^{3+} ion transitions.

The decay lifetimes measured at three emission wavelengths, 478, 540 and 651 nm, by exciting at 980 nm (pulse length: 5 ns and 5 ms between two pulses) are plotted in Fig. 8 as a function of heat-treatment time (log scale). The observed decay-time behavior (not presented here) follows a single-exponential decay for all of the samples.

The lifetimes measured for the blue transition at 478 nm and attributed to the Tm^{3+}: $[^1G_4 \rightarrow {}^3H_6]$ and Er^{3+}: $[^4F_{7/2} \rightarrow {}^4I_{15/2}]$ radiative transitions range from 60 to 70 µs and do not exhibit any significant change with thermal treatment duration. In contrast, a sharp increase of the lifetime from 22 to 60 µs for the 540 nm emission (ascribed to the Er^{3+}: $[^4S_{3/2} \rightarrow {}^4I_{15/2}]$ transition) and from 66 to 184 µs for the 651 nm emission (attributed to both Er^{3+}: $[^4F_{9/2} \rightarrow {}^4I_{15/2}]$ and Tm^{3+}: $[^1G_4 \rightarrow {}^3F_4]$ transitions) can be observed in Fig. 8 from 2 to 6 h of heat-treatment. For longer heat-treatment durations, *i.e.* from 10 h to 170 h, the lifetime of both green and red transitions slightly increases, as shown in Fig. 8.

4. Discussion

4.1 Structural investigation

In our previous work on Er^{3+} and Yb^{3+} codoped NYBC glasses and glass-ceramics,[36] we have shown the repeatability as well as the stoichiometry conservation of the synthesis procedure utilized here. Moreover, the structural investigation of the crystallization process performed in that previous work through X-ray diffraction and scanning electron microscopy has revealed the formation of fluorite-type cubic crystals without clear identification of its composition among the three isomorphs CaF_2, $Ca_{1-x}Y_xF_{2+x}$ and α-$NaYF_4$. CaF_2 is a well-known model describing the cubic fluorite crystalline structure, where fluoride anions F^- occupy the tetrahedral sites in the fcc lattice of calcium Ca^{2+} cations. Then, the $Ca_{1-x}Y_xF_{2+x}$ belongs to the $(CaF_2)_{1-x}$–$(YF_3)_x$ solid solution where fluorite-type crystals exist when x is comprised between 0 to 0.35.[41] Lastly, the $NaYF_4$ crystal consists of two polymorphs: the cubic fluorite phase, labeled α-$NaYF_4$ and the hexagonal one, labeled β-$NaYF_4$.[42,43] The former is generally known to be formed only at high temperature while the latter is the stable phase at low temperature.[43] However, no evidence of the presence of the hexagonal β-$NaYF_4$ phase was observed here from the X-ray diffraction analyses. Besides, the formation of the cubic α-$NaYF_4$ at low temperature was previously observed in a fluoro-silicate glass-ceramic and attributed to the metastable character of the glassy state.[35] The X-ray diffraction patterns recorded on the triply doped NYBC-4 glass-ceramics up to 3 h of heat-treatment (Fig. 3(a)) are identical to those reported in our previous work, suggesting the same crystallization of the cubic fluorite-type phase, as further illustrated by the electron microscopy images presented in Fig. 4.

In contrast to our results presented in ref. 36 where long heat-treatments have resulted in a complex uncontrolled crystallization leading to opaque glass-ceramics, a high visible transparency of the NYBC-4 glass-ceramics was maintained in the present work, even after 170 h of thermal treatment (see Fig. 2). This is readily explainable by the lower temperature used here for the ceramization process (380 °C *vs.* 400 °C in ref. 36), which has permitted us to retain the crystal size around 100 nm

Published on 07 April 2014. Downloaded by UNIVERSIDAD SAO PAULO on 23/06/2014 15:15:39.

and to avoid any uncontrolled growth, as shown by both SEM and TEM images in Fig. 4. Besides the major role played by the crystalline particle size toward the transparency of glass-ceramics, the difference of the refractive index between crystals and glass is also an important factor to consider, according to Rayleigh's theory. The reported linear refractive index of fluoride crystalline phases (n_D, at 589 nm) is 1.434 for CaF_2,[44] 1.430 for $NaYF_4$,[43] and 1.48 for $Ca_{1-x}Y_xF_{2+x}$ ($x = 0.25$)[45] while the refractive index measured here on the NYBC-4 glass at 633 nm is 1.538. The relatively weak difference of the refractive index between both media is thus determinant here with regard to the GC-170 h transparency if we consider that its crystal size (~100 nm) is slightly larger than that usually reported in transparent oxyfluoride glass-ceramics (<40 nm).[46]

4.2 Optical properties

In order to determine the optical band gap of the prepared samples, their linear absorption coefficient was, for the first time, determined from their transmission spectrum according to:

$$\alpha(\upsilon) = -\frac{\ln(T)}{d} \quad (1)$$

where T is the optical transmission as a function of frequency υ and d is the glass thickness (here, $d = 1.5$ mm). Then, direct and indirect optical bandgaps and Urbach energy were calculated *via*:

$$\alpha(h\upsilon) = A\frac{(h\upsilon - E_{opt})^p}{h\upsilon} \quad (2)$$

where A is a constant called band tailing parameter, E_{opt} is the optical band gap, h is the Planck constant and p is an index depending on the nature of the electronic transitions responsible for the absorption ($p = 0.5$ for E_{dir} and $p = 2.0$ for E_{indir}).[47] Lastly, the absorption coefficient near the band edge shows an exponential dependence on photon energy and this dependence is given as follows:[48]

$$\alpha(h\upsilon) = \alpha_0 \exp\left(\frac{h\upsilon}{E_U}\right) \quad (3)$$

where α_0 is a constant and E_U is the Urbach energy that can be interpreted as the width of the valence band tails of localized states, associated with the structural disorder of the amorphous state. The calculated optical band gaps (E_{dir} and E_{indir}) and Urbach energy E_U are plotted in Fig. 9 as a function of heat-treatment time. It clearly appears that thermal-treatment of the samples results in a nonlinear decrease and increase of their optical band gap and Urbach energy E_U, respectively. No further significant change of those energies is observed after 16 hours of heat-treatment, as shown by the almost identical transmission spectra of GC-16 h and GC-170 h in Fig. 2. Note that the calculated energies for the GC-170 h sample are not plotted in Fig. 9 for better clarity. We can thus assume that the crystallization in this material reaches a limit after 16 hours of treatment after which no significant increase of crystallization volume occurs, as shown by both the GC-170 h transmission

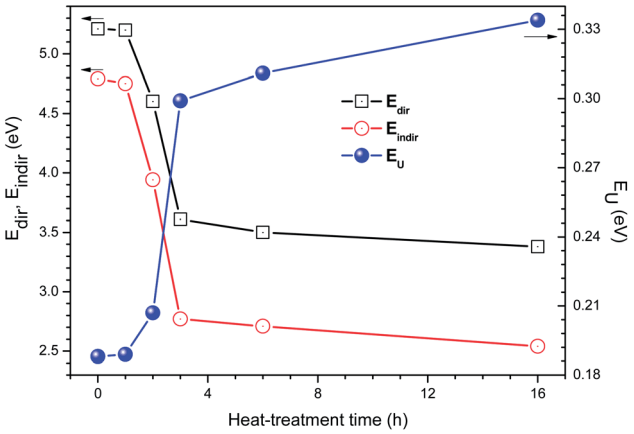

Fig. 9 Optical band gap (E_{dir} and E_{indir}) and the E_U as a function of the heat-thermal time. Lines are guides to the eye.

spectrum (Fig. 2) and up-conversion emissions intensity (Fig. 7) which are close to that of the GC-16 h sample.

A significant change of the relative intensities of the emission bands in the NYBC-4 glass and GC-170 h glass-ceramic can be observed in Fig. 5 and 6, respectively. In frequency up-conversion processes, it is well established that the up-conversion emission intensity I_{UC} is proportional to the excitation intensity I_{exct} according to $I_{UC} \propto (P_{exct})^n$, where n accounts for the number of excitation infrared photons involved in the excitation mechanism. The number n is necessarily an integer and is deduced from the slope of the straight line obtained by plotting $\log(I_{UC})$ *vs.* $\log(P_{exct})$, as presented in the inset of Fig. 5 and 6, for the NYBC-4 glass and GC-170 h glass-ceramic, respectively. All the regression curves were obtained with an R-square value higher than 0.99, indicating an excellent accuracy of the fits, as shown as well by the standard error values calculated for each slope and reported in the respective legends. First, if we consider the violet and green well-known emissions of Er^{3+} ions, the slopes obtained from the $\log(I_{UC})$ *vs.* $\log(P_{exct})$ plot for the transitions $^2H_{9/2} \rightarrow {}^4I_{15/2}$ (406 nm), $^2H_{11/2} \rightarrow {}^4I_{15/2}$ (520 nm) and $^4S_{3/2} \rightarrow {}^4I_{15/2}$ (540 nm) are respectively 2.88, 2.37 and 2.06 for the 170 h glass-ceramic. For the glass, the violet emission at 406 nm was too weak to measure accurately its intensity while slopes of 2.49 and 2.45 were obtained for the 520 and 540 nm emission bands, respectively. Therefore, these results indicate that the green (520 and 542 nm) emissions are related to a two-photon process while the violet emission (406 nm) can be ascribed to a three-photon process, which is coherent with similar studies reported in the literature.[49–51]

Then, the attribution of the red emission observed at 651–667 nm is ambiguous because both Er^{3+} and Tm^{3+} ions may emit in this region. First, for the Er^{3+} ion, the involved transition may be $^4F_{9/2} \rightarrow {}^4I_{15/2}$. This emission was observed with a peak centered at 667 nm in the Tm^{3+}-free glass and glass-ceramics of the same composition.[36] Second, the transition $^1G_4 \rightarrow {}^3F_4$ of Tm^{3+} ions may also contribute to the red emission, as already reported in the literature.[25] From the normalized emission spectra presented in Fig. 1, we observe a slight increase of the intensity of the red emission with increasing content of Tm^{3+}

 This journal is © The Royal Society of Chemistry 2014

Published on 07 April 2014. Downloaded by UNIVERSIDAD SAO PAULO on 23/06/2014 15:15:39.

from 2 to 4 wt%. Nevertheless, almost no change is observed between the glasses containing 1 and 2 wt%. At this point, we can thus only assume that both Er^{3+} and Tm^{3+} ions are involved in the red emission, with a probable greater contribution of the latter ions. From the double log plot of the emission intensity *vs.* excitation power at 651 nm in glass and glass-ceramic (inset of Fig. 5 and 6), a two-photon excitation process may be assumed. On the other hand, the blue emissions at 450 and 478 nm and the near infrared emission at 795 nm observed in Fig. 5 and 6 can be unambiguously ascribed to the following transitions of Tm^{3+} ions: $^1D_2 \rightarrow {}^3F_4$ (450 nm), $^1G_4 \rightarrow {}^3H_6$ (478 nm), and $^3H_4 \rightarrow {}^3H_6$ (795 nm), with respective obtained slopes close to 3 and 2 in both the glass and the glass-ceramic treated for 170 h. The blue emissions can be thus ascribed to a three-photon excitation process and the near infrared one (781 nm) to a two-photon mechanism.

In Fig. 7, the plot of intensity ratios $I_{\text{glass-ceramic}}/I_{\text{glass}}$ for each emission band under excitation at 975 nm (laser diode power of 30 mW) as a function of heat-treatment duration shows the influence of crystallization rate on the REI emission. One can clearly observe from Fig. 7 that the intensity of the Er^{3+} emission bands strongly increases – of about 170 times for the 406 nm violet transition and 10 to 20 times for the green transitions – whereas the Tm^{3+} main emission band at 478 nm remains unchanged.

Different mechanisms are involved in the up-conversion emission processes to excite the Er^{3+} levels $^2H_{9/2}$, $^4F_{\{3/2-9/2\}}$, $^2H_{11/2}$, $^4S_{3/2}$ and $^4I_{9/2}$ as well as the Tm^{3+} levels $^1D_2$, $^1G_4$, $^3F_{\{2-3\}}$ and $^3H_4$ in the presence of Yb^{3+} sensitizer ions upon laser excitation at 975 nm. Here, four excitation mechanisms can be distinguished: energy transfer up-conversion (ET), ground state absorption (GSA), excited state absorption (ESA) and cross-relaxation (CR). Due to the large absorption cross-section of Yb^{3+} ions around 975 nm, the expected dominant process is the energy transfer (ET) from the excited level $^2F_{5/2}$ of Yb^{3+} to the Er^{3+} levels: $^4I_{11/2}$, $^4F_{7/2}$, $^4I_{13/2}$ and $^4F_{9/2}$ (respectively labeled ET{1–4}E in Fig. 10) on one hand, and to the Tm^{3+} levels: $^3H_5$, $^3F_4$, $^3H_4$ and $^1G_4$ (respectively labeled ET{1–4}T in Fig. 10) on the other hand. Besides, the excitation of the $^1D_2$ state is also possible from the $^3H_4$ state through a CR process. The different possible excitation–emission mechanisms are resumed in the simplified energy diagram presented in Fig. 10 where the optical band gap of the GC-2 h and GC-170 h samples is also depicted.

We can assume that the separation distance between Yb^{3+} and Tm^{3+} ions is less than that between Yb^{3+} with Er^{3+} ions due to the initial REI concentrations. Thus, the ET probability between the REI in the glass and GC samples is first governed by $Yb^{3+} \rightarrow Tm^{3+}$ and then by $Yb^{3+} \rightarrow Er^{3+}$.

According to this criterion, the excitation–emission pathways of the Tm^{3+} ions are: (i) population of the $^3H_5$ level *via* the energy transfer ET1T followed by a non-radiative (NR) relaxation to the $^3F_4$ level and the excited state absorption from this level ESA1 (resulting from ET2T) to populate the $^3F_{2-3}$ levels, the radiative relaxation from the $^3F_2$ level leads to red emission (651 nm), (ii) the $^3H_4$ level can be populated by NR relaxation from the $^3F_{2-3}$ levels and then radiatively decays by emitting at approximately 800 nm; (iii) the $^1G_4$ level can be excited by two ways, by the ESA2 from the $^3H_4$ level (resulting from ET3T) or *via* the two-photon absorption (TPA) at 975 nm from two Yb^{3+} ions, two main radiative decays can then occur from the excited $^1G_4$ state: the first one to the excited level $^3F_4$, with a red emission at 651 nm, and the second one to the ground state $^3H_6$, giving rise to the blue emission at 478 nm; (iv) at last, we can observe the ESA3 from the $^1G_4$ level (resulting from ET4T) which will populate the $^1D_2$ level and then be followed by a radiative transition to the excited level $^3F_4$ centered at 450 nm. The latter transition will depend on the optical band gap of the sample, as the Tm^{3+}: [$^1D_2$] energy level is located within the conduction band (Fig. 10).

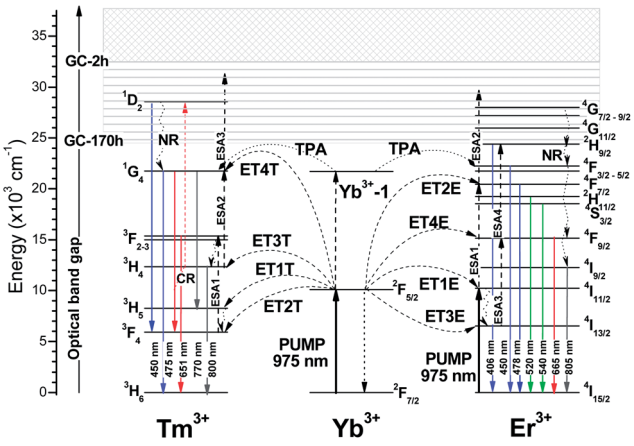

Fig. 10 Simplified energy level diagram of Yb^{3+}, Er^{3+} and Tm^{3+} ions with the main transitions describing the up-conversion luminescence, and the optical band gap for the GC-2 h and GC-170 h samples, respectively. (Yb^{3+}-1 represents a second Yb^{3+} ion.)

Regarding the Er^{3+} ion transitions, the excitation pathways are: (i) the population of the $^4I_{11/2}$ level by both GSA and ET1E, explaining its usually observed prolonged lifetime,[52] which can be followed by both a NR relaxation to the $^4I_{13/2}$ level or the ESA1 which will populate the $^4F_{7/2}$ level; (ii) from the excited $^4F_{7/2}$ level, the population of the $^4G_{7/2-11/2}$ level can occur through the ESA2 (resulting from ET2E), depending on the optical band gap (see Fig. 10); (iii) besides, the $^4F_{7/2}$ level can be populated *via* the TPA from two Yb^{3+} ions; (iv) the $^4F_{9/2}$ and $^2H_{9/2}$ levels can be excited consecutively from the $^4I_{13/2}$ and $^4F_{9/2}$ excited states by ESA3 and ESA4, respectively (both due to ET3E and ET4E, respectively). All these excitations may then result in the following radiative transition from the excited levels $^2H_{9/2}$, $^4F_{3/2-7/2}$, $^2H_{11/2}$–$^4S_{3/2}$, $^4F_{9/2}$ and $^4I_{9/2}$ to the ground state $^4I_{15/2}$, leading to the violet (406 nm) emission, blue (~450 to 478 nm) emissions, green (~520 to 540 nm) emissions, red (665 nm) and near-infrared (805 nm) emissions, respectively.

From Fig. 7 as well as the emission spectra presented in Fig. 5 and 6 for the NYBC-4 glass and GC-170 h, respectively, we can note that: (i) the intensity of the violet emission (Er^{3+}: [$^2H_{9/2} \rightarrow {}^4I_{15/2}$]) has a much higher (up to 160 times) increment upon thermal treatment which can be related to the optical band gap (Fig. 9) favoring both ESA3 processes; (ii) the intensities of the blue emission (Er^{3+}: [$^4F_{3/2-7/2} \rightarrow {}^4I_{15/2}$] + Tm^{3+}: [$^1D_2 \rightarrow {}^3F_4 + {}^1G_4 \rightarrow {}^3H_6$]) and the green emission (Er^{3+}: [$^2H_{11/2}$, $^4S_{3/2} \rightarrow {}^4I_{15/2}$]) are

Published on 07 April 2014. Downloaded by UNIVERSIDAD SAO PAULO on 23/06/2014 15:15:39.

increased respectively by about 5 and 10 times in the glass-ceramics when compared to the glass; (iii) the intensity of the red emission (Er^{3+}: $[^4F_{9/2} \rightarrow {}^4I_{15/2}] + Tm^{3+}$: $[^3F_{2-3} \rightarrow {}^3H_6 + {}^1G_4 \rightarrow {}^3F_4]$, due to ESA3 and, ESA1 + ESA2, respectively) is improved by about 12 times and; (iv) the intensity of the near-infrared band at 795 nm (Er^{3+}: $[^4I_{9/2} \rightarrow {}^4I_{15/2}] + Tm^{3+}$: $[^1G_4 \rightarrow {}^3H_5 + {}^3H_4 \rightarrow {}^3H_6]$) almost does not evolve as a function of heat-treatment time.

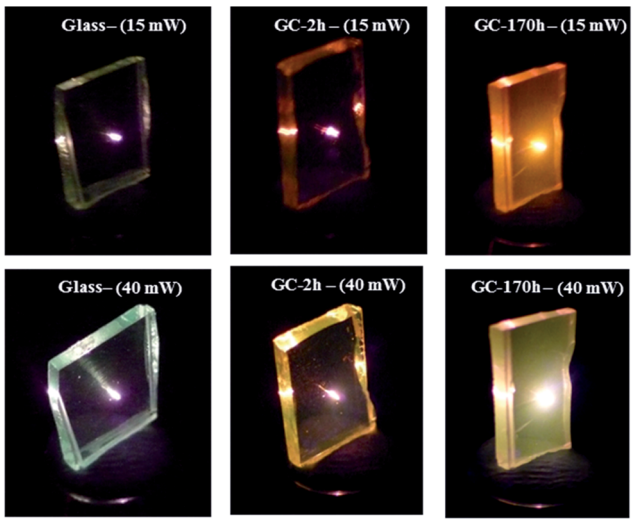

Fig. 11 Photographs of the NYBC-4 glass and the GC-2 h and GC-170 h glass-ceramics excited at 975 nm with a diode power of 15 and 40 mW.

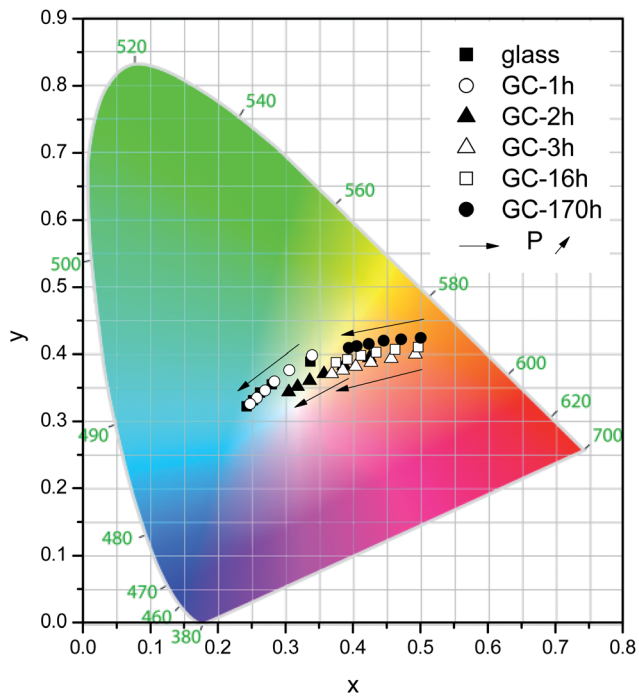

Fig. 12 Chromaticity diagram showing the calculated coordinates of NYBC-4 glass and glass-ceramics as a function of heat-treatment time and laser diode power at 975 nm ranging from 15 to 40 mW.

Therefore, if one neglects the ET processes between energy levels of similar energy and considers that all the ET processes occur from the excited Yb^{3+} ions to the Er^{3+} and Tm^{3+} acceptor ions, in addition to the ESA processes, then a multicolor up-conversion emission can be achieved from the NYBC-4 glass and glass-ceramics, as illustrated in Fig. 11 and 12. Besides, control of the ceramization process and pumping power at 975 nm allow the intensity of the three RGB emission bands to be modulated.

The chromaticity diagram presented in Fig. 12 shows the color rendering tuning obtained from the glass and glass-ceramics for different heat-treatment durations by increasing the 975 nm laser diode excitation power from 15 to 40 mW, as indicated by the arrow for each sample. The images presented in Fig. 11 are photographs displaying the different colors emitted by the glass and GC-2 h and GC-170 h glass-ceramics when excited at 15 and 40 mW at 975 nm.

5. Conclusions

In summary, Yb^{3+}, Er^{3+} and Tm^{3+} triply doped $(NaPO_3)_{40}$–$(YF_3)_{30}$–$(BaF_2)_{20}$–$(CaF_2)_{10}$ fluoro-phosphate glasses have been prepared with a view to generate white light through the addition of red, green and blue (RGB) emission bands of the rare earth ions (REI) *via* an excitation in the near infrared range at 975 nm. The optimal REI concentrations for this purpose were determined to be 4 wt% of YbF_3, 2 wt% of ErF_3 and 4 wt% of TmF_3. Then, highly transparent and optically homogeneous glass-ceramics have been reproducibly fabricated by heat-treatment of the selected glass composition above their glass transition temperature, resulting in optical direct and indirect band gap changes and modification of their luminescence properties. The formation of cubic fluorite-type nanocrystals homogeneously dispersed within the volume has been evidenced and characterized at the early stage of the crystallization process through X-ray diffraction (*in situ* and *ex situ* powder techniques) and electron microscopies as well. A large improvement of the up-conversion emission intensity – from 10 to 170 times larger – has been measured in the glass-ceramics when compared to the parent glass, confirming the role played by the ceramization process in incorporating the REI into a more structured (crystalline) environment. Moreover, significant changes in the relative intensities of the violet, blue, green and red emissions upon 975 nm laser diode excitation have been observed as a function of the applied heat-treatment duration and laser excitation power. Such features are also attributed to the incorporation of REI into the nanocrystals and give rise to a wide range of designable color rendering (from orange to turquoise through white, according to the CIE-1931 standards) by only controlling the laser excitation power and the crystallization rate of a single bulk material. Such wide emission tunability obtained, thanks to the excellent ability of these fluoro-phosphate glasses to form homogeneous transparent glass-ceramics, makes these materials promising candidates for application in solid-state lighting, solar cell technology and other active photonic devices.

This journal is © The Royal Society of Chemistry 2014

Published on 07 April 2014. Downloaded by UNIVERSIDAD SAO PAULO on 23/06/2014 15:15:39.

Acknowledgements

The authors are grateful to the Canadian Excellence Research Chair program (CERC) on Enabling Photonic Innovations for Information and Communication for financial support. The Brazilian agencies FAPESP, CNPq through the INOF/CEPOF (Instituto Nacional de Óptica e Fotônica and Centro de Pesquisa em Óptica e Fotônica – São Paulo - Brazil) and the French ANR (project CrystOG ANR-12-JS08-0002-01) are also acknowledged.

Notes and references

1 T. L. Dawson, *Color. Technol.*, 2010, **126**, 1–10.
2 M. R. Krames, O. B. Shchekin, R. Mueller-Mach, G. O. Mueller, L. Zhou, G. Harbers and M. G. Craford, *J. Disp. Technol.*, 2007, **3**, 160–175.
3 J. de Wild, A. Meijerink, J. K. Rath, W. van Sark and R. E. I. Schropp, *Energy Environ. Sci.*, 2011, **4**, 4835–4848.
4 W. Holand and G. H. Beall, *Glass ceramic technology*, Wiley and sons, 2nd edn, 2012.
5 M. Mortier, *Philos. Mag. B*, 2002, **82**, 745–753.
6 A. de Pablos-Martin, A. Duran and M. J. Pascual, *Int. Mater. Rev.*, 2012, **57**, 165–186.
7 L. Calvez, H. L. Ma, J. Lucas and X. H. Zhang, *Adv. Mater.*, 2007, **19**, 129–132.
8 A. C. Yanes, A. Santana-Alonso, J. Mendez-Ramos, J. del-Castillo and V. D. Rodriguez, *Adv. Funct. Mater.*, 2011, **21**, 3136–3142.
9 A. Herrmann, M. Tylkowski, C. Bocker and C. Ruessel, *Chem. Mater.*, 2013, **25**, 2878–2884.
10 Y. Teng, K. Sharafudeen, S. F. Zhou and J. R. Qiu, *J. Ceram. Soc. Jpn.*, 2012, **120**, 458–466.
11 S. Nagpal, *J. Nanopart. Res.*, 2011, **13**, 2733–2741.
12 F. Wang and X. Liu, *Chem. Soc. Rev.*, 2009, **38**, 976–989.
13 J. F. Suyver, A. Aebischer, D. Biner, P. Gerner, J. Grimm, S. Heer, K. W. Kramer, C. Reinhard and H. U. Gudel, *Opt. Mater.*, 2005, **27**, 1111–1130.
14 R. X. Yan and Y. D. Li, *Adv. Funct. Mater.*, 2005, **15**, 763–770.
15 C. Cao, W. Qin, J. Zhang, Y. Wang, G. Wang, G. Wei, P. Zhu, L. Wang and L. Jin, *Opt. Commun.*, 2008, **281**, 1716–1719.
16 F. Wang, Y. Han, C. S. Lim, Y. H. Lu, J. Wang, J. Xu, H. Y. Chen, C. Zhang, M. H. Hong and X. G. Liu, *Nature*, 2010, **463**, 1061–1065.
17 V. Mahalingam, F. Mangiarini, F. Vetrone, V. Venkatramu, M. Bettinelli, A. Speghini and J. A. Capobianco, *J. Phys. Chem. C*, 2008, **112**, 17745–17749.
18 J. Yang, C. Zhang, C. Peng, C. Li, L. Wang, R. Chai and J. Lin, *Chem.– Eur. J.*, 2009, **15**, 4649–4655.
19 N. Niu, P. Yang, F. He, X. Zhang, S. Gai, C. Li and J. Lin, *J. Mater. Chem.*, 2012, **22**, 10889–10899.
20 A. S. Gouveia-Neto, L. A. Bueno, R. F. do Nascimento, E. A. da Silva, E. B. da Costa and V. B. do Nascimento, *Appl. Phys. Lett.*, 2007, **91**, 091114.
21 E. Downing, L. Hesselink, J. Ralston and R. Macfarlane, *Science*, 1996, **273**, 1185–1189.
22 H. T. Bookey, J. Lousteau, A. Jha, N. Gayraud, R. R. Thomson, N. D. Psaila, H. Li, W. N. MacPherson, J. S. Barton and A. K. Kar, *Opt. Express*, 2007, **15**, 17554–17561.
23 Y. Ledemi, D. Manzani, S. J. L. Ribeiro and Y. Messaddeq, *Opt. Mater.*, 2011, **33**, 1916–1920.
24 D. Q. Chen, Y. S. Wang, K. L. Zheng, T. L. Guo, Y. L. Yu and P. Huang, *Appl. Phys. Lett.*, 2007, **91**, 251903.
25 J. Mendez-Ramos, V. D. Rodriguez, V. K. Tikhomirov, J. del-Castillo and A. C. Yanes, *Eur. Phys. J.: Appl. Phys.*, 2008, **43**, 149–153.
26 S. F. Leon-Luis, J. Abreu-Afonso, J. Pena-Martinez, J. Mendez-Ramos, A. C. Yanes, J. del-Castillo and V. D. Rodriguez, *J. Alloys Compd.*, 2009, **479**, 557–560.
27 K. Hirao, K. Tanaka, M. Makita and N. Soga, *J. Appl. Phys.*, 1995, **78**, 3445–3450.
28 L. A. Bueno, P. Melnikov, Y. Messaddeq and S. J. L. Ribeiro, *J. Non-Cryst. Solids*, 1999, **247**, 87–91.
29 F. Auzel, D. Pecile and D. Morin, *J. Electrochem. Soc.*, 1975, **122**, 101–107.
30 Y. H. Wang and J. Ohwaki, *Appl. Phys. Lett.*, 1993, **63**, 3268–3270.
31 M. Abril, J. Mendez-Ramos, I. R. Martin, U. R. Rodriguez-Mendoza, V. Lavin, A. Delgado-Torres, V. D. Rodriguez, P. Nunez and A. D. Lozano-Gorrin, *J. Appl. Phys.*, 2004, **95**, 5271–5279.
32 V. K. Tikhomirov, D. Furniss, A. B. Seddon, I. M. Reaney, M. Beggiora, M. Ferrari, M. Montagna and R. Rolli, *Appl. Phys. Lett.*, 2002, **81**, 1937–1939.
33 X. S. Qiao, X. P. Fan, J. Wang and M. Q. Wang, *J. Non-Cryst. Solids*, 2005, **351**, 357–363.
34 S. Tanabe, H. Hayashi, T. Hanada and N. Onodera, *Opt. Mater.*, 2002, **19**, 343–349.
35 F. Liu, E. Ma, D. Chen, Y. Yu and Y. Wang, *J. Phys. Chem. B*, 2006, **110**, 20843–20846.
36 Y. Ledemi, M. El Amraoui, J. L. Ferrari, P.-L. Fortin, S. J. L. Ribeiro and Y. Messaddeq, *J. Am. Ceram. Soc.*, 2013, **96**, 825–832.
37 CIE colorimetry (International Commission on Illumination).
38 D. Taylor, *Trans. J. Br. Ceram. Soc.*, 1984, **83**, 92–98.
39 P. A. Santa-Cruz and F. S. Teles, *Spectra Lux Software v.1.0, Ponto Quântico Nanodispositivos/RENAMI*, 2003.
40 T. N. Blanton and L. S. Hung, *Powder Diffr.*, 1996, **11**, 204–208.
41 K. Seirania, P. P. Fedorov, L. Garashin, G. V. Molev, V. V. Karelin and B. P. Sobolev, *J. Cryst. Growth*, 1974, **26**, 61–64.
42 Z. J. Wang, F. Tao, L. Z. Yao, W. L. Cai and X. G. Li, *J. Cryst. Growth*, 2006, **290**, 296–300.
43 R. E. Thoma, G. M. Hebert, H. Insley and C. F. Weaver, *Inorg. Chem.*, 1963, **2**, 1005–1012.
44 I. H. Malitson, *Appl. Opt.*, 1963, **2**, 1103–1107.
45 D. M. Roy and R. Roy, *J. Electrochem. Soc.*, 1964, **111**, 421–429.
46 M. Mortier and G. Dantelle, in *Functionalized Inorganic Fluorides*, ed. P. Garcia Juan, H.-W. Swidersky, T. Schwarze and J. Eicher, John Wiley & Sons, Ltd, 2010, pp. 205–228.

47 E. A. Davis and N. F. Mott, *Philos. Mag.*, 1970, **22**, 903–922.
48 F. Urbach, *Phys. Rev.*, 1953, **92**, 1324.
49 X. Qiao, X. Fan, M. Wang, J.-L. Adam and X. Zhang, *J. Phys.: Condens. Matter*, 2006, **18**, 6937–6951.
50 L. Y. Zhang, H. T. Sun, S. Q. Xu, K. F. Li and L. L. Hu, *Solid State Commun.*, 2005, **135**, 449–454.
51 M. Liao, L. Hu, Y. Fang, J. Zhang, H. Sun, S. Xu and L. Zhang, *Spectrochim. Acta, Part A*, 2007, **68**, 531–535.
52 *Rare-earth doped fiber lasers and amplifiers, revised and amplified*, ed. M. J. F. Digonnet, CRC Press, 2001.

Published on 07 April 2014. Downloaded by UNIVERSIDAD SAO PAULO on 23/06/2014 15:15:39.

This journal is © The Royal Society of Chemistry 2014